Electrical and Thermal Performance Analysis of AlGaN/GaN HEMT without Voltage-Blocking Buffer Layer Design

Chong Rong Huang[1], Hsien-Chin Chiu[1], Chia-Hao Liu[1], Hsiang-Chun Wang[1], Chao-Wei Chiu[1], Hsuan-Ling Kao[1], Chih-Tien Chen[2], and Kuo-Jen Chang[2]

[1]Department of Electronics Engineering, Chang Gung University, Taoyuan 333, Taiwan

[2]National Chung-Shan Institute of Science and Technology, Materials and Electro-Optics Research Division, Taoyuan 333, Taiwan

Email: hcchiu@mail.cgu.edu.tw

Keywords: GaN HEMT, no buffer, high-quality AlN nucleation layer, thermal effect, pulse measurements, thermal image measurements

Abstract

The electrical and thermal performance of a no-buffer layer AlGaN/GaN high-electron-mobility transistor (on a SiC substrate for radio frequency devices is reported in this study. The no-buffer structure has excellent pulse measurement characteristics, and the current collapse at a drain quiescent voltage of 30 V is 3%. Compared with the conventional thick buffer layer, the high structural quality nucleation layer and no-buffer layer structure can reduce the thermal boundary resistance and self-heating when the device operates at a high drain bias. In thermal imaging measurements, the no-buffer device exhibits higher power and lower surface temperature at the same gate-to-source voltage and drain voltage as the standard device. Because the no-buffer structure improves the DC characteristics of the device and reduces the current collapse effect, that device has better small signal and linearity characteristics and a lateral breakdown voltage of 1900 V.

INTRODUCTION

In recent years, the market demand for high-frequency and high-power devices has increased. Therefore, the semiconductor gallium nitride (GaN) with its larger bandgap has the advantages of small size, high power, and low loss, which are ideal for high speed chargers, 5G communications, electric vehicles, and other higher power applications. For these, GaN on silicon carbide(SiC) has better performance than GaN on silicon in electronic applications. Therefore, in the past two decades, many GaN-on-SiC electronic devices have been developed.

Commonly used GaN high-electron-mobility transistors (HEMTs) are typically grown on sapphire, silicon(Si), SiC, or native GaN substrates. The market is dominated by Si substrates for cost reasons, but Si substrates have poor heat dissipation and thermal expansion characteristics. For high-power and high-frequency devices, SiC with its high thermal conductivity and better lattice matching is typically chosen as a substrate to achieve better output power and high-frequency characteristics.

The lattice mismatch between GaN and the substrate will increase defect density and affect reliability. A common method for reducing the lattice mismatch and defect density is to grow an AlN nucleation layer (NL) and dope a deep GaN buffer layer with acceptors such as Fe [1-3] or C [4-6]. However, a thick GaN buffer layer will affect the overall thermal resistance of the device and weaken the heat dissipation advantage of the SiC substrate. These deep acceptors also cause electron-trapping or current collapse, degrading the HEMT performance. Therefore, a no-buffer structure based on QuanFINE [7] is reported in this study. This structure can not only reduce the current collapse effect caused by the buffer layer but also improve the reliability of the device by using AlN as a back barrier layer.

EXPERIMENTAL PROCEDURES

The AlGaN/GaN HEMT was grown on 6-inch SiC substrates with metal-organic chemical vapor deposition (MOCVD). The standard device has a conventional 55 nm AlN NL and 1.7-μm buffer layer. However, a few studies have shown that defects in the NL are likely to increase the thermal boundary resistance (TBR), increasing the temperature of the device channel layer [7-9]. Therefore, in this study, a high epitaxial quality 55 nm AlN NL was grown by hot-wall MOCVD to reduce the TBR effect and improve the channel temperature of the device. A 0.5 nm thick AlN spacer layer was grown between the 300 nm GaN channel layer and the 18 nm thick $Al_{0.24}Ga_{0.86}N$-barrier layer. Finally, a 2 nm GaN cap was deposited through MOCVD.

Low-TBR no-buffer layer AlGaN/GaN HEMTs were fabricated on 6-inch SiC substrates, and their schematic cross-sections are shown in Fig. 1(b). Fig. 1(c) shows the scanning transmission electron microscope (STEM) cross-sections of the GaN-on-SiC, and Fig. 1(a) is energy-dispersive X-ray spectroscopy (EDS) results. The radio frequency (RF) device has a gate length L_G of 0.25 μm, a gate–source distance L_{GS} of 0.75 μm, and a gate–drain distance L_{GD} of 2.25 μm.

In Fig. 2, the typical full width at half maximum (FWHM) value of X-ray diffraction (XRD) for the GaN (002) and (102) reflections of the no-buffer and standard devices were 175/372 and 184/390 arcsec, respectively. The dislocation density was calculated using the XRD FWHM results as 8.0 × 10^8/cm^2, and that of the standard device was 8.8 × 10^8/cm^2.

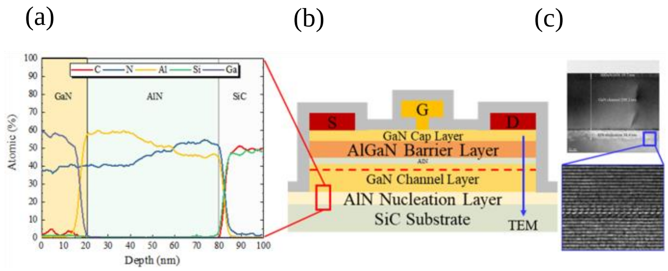

Fig. 1. (a) EDS line scan, (b) schematic process cross-section, and (c) STEM overview image of no-buffer device.

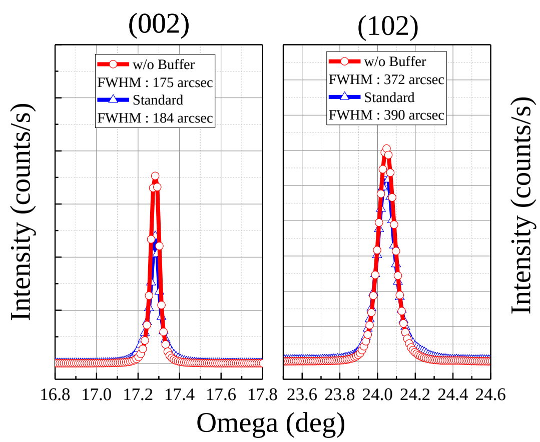

XRD	FWHM (002) (arcsec)	FWHM(102) (arcsec)	Dislocation(screw) (cm^{-2})	Dislocation(edge) (cm^{-2})	Dislocation(total) (cm^{-2})
no-buffer	175	372	6.2×10^7	7.4×10^8	8.0×10^8
Standard	184	390	6.8×10^7	8.1×10^8	8.8×10^8

Fig. 2. XRD results and total dislocation of no-buffer and standard devices.

RESULTS AND DISCUSSION

We measured the DC and small-signal characteristics of the devices by using an Agilent 4142B and Agilent 8643C network analyzer to study the effect of a high-quality AlN NL and a no-buffer layer structure on the performance of the device. Fig. 3 (a) shows the drain-to-source current (I_{DS}) and output transconductance (g_m) versus gate-to-source voltage (V_{GS}) at V_{DS} of 10 V, with a V_{GS} sweep from −6 V to 2 V. The saturation currents of the no-buffer and standard devices were 1215 and 1076 mA/mm, respectively, at V_{GS} = 2 V and V_{DS} = 10 V. To better observe the self-heating effect of the device, we measured the I_{DS}–V_{DS} characteristics. According to the results shown in Fig. 3(b), the saturation currents for the I_{DS} of the no-buffer and standard devices were 1103 and 895 mA/mm at a drain voltage up to V_{DS} = 28 V. The high-quality AlN NL and no-buffer layer structure devices have less current decay in a high-power state. The ON-resistance (R_{on}) values of the two devices were seen to be 2.9 ($R_{on\_no\text{-}buffer}$) and 3.4 Ω·mm ($R_{on\_standard}$).

In the small-signal measurements, we measured the S-parameters of both devices from 100 MHz to 50 GHz using an Agilent network analyzer, as shown in Fig. 3(c). The results show that the maximum current gain cut-off frequency (f_T) and maximum frequency of oscillation (f_{max}) of the device no-buffer were f_T/f_{max} = 31/75 GHz, respectively. On the other hand, the f_T/f_{max} values of the standard device were 27.7/65.9 GHz.

To explore the influence of ambient temperature on the device characteristics, we performed variable temperature measurements on the two devices. Fig. 3(d) illustrates the small-signal measurements from 300 to 400 K with a 25 K step. The f_{max} of the no-buffer device decreases at a rate of 0.26 GHz/K, whereas the standard device decreases at a rate of 0.34 GHz/K as the temperature increases. Compared with the standard device, the no-buffer structure reduces the additional thermal boundary resistance caused by phonon scattering at high temperatures due to the high-quality AlN NL [12].

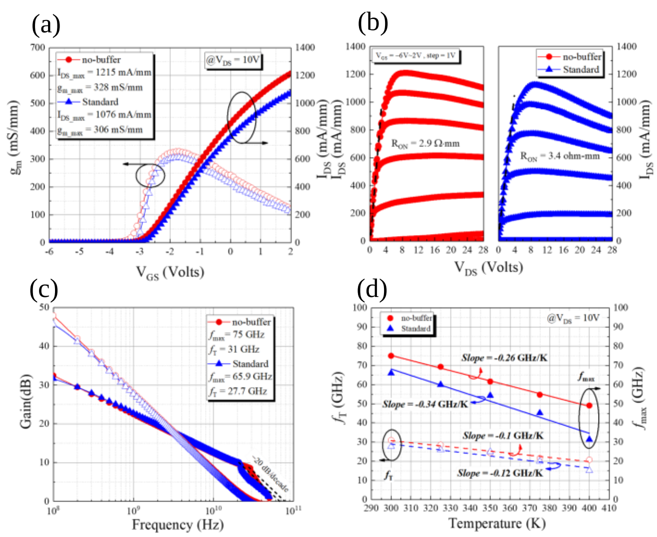

Fig. 3. (a) Transfer characteristics (I_{DS}–V_{GS}) at V_{DS} = 10 V with a V_{GS} sweep from −6 to 2 V; (b) I_{DS}–V_{DS} Output current; (c) small-signal characteristics, and (d) temperatures of the two devices.

The pulse I_{DS}–V_{DS} measurements of the two devices by using AMCAD-241 are depicted in Fig. 4. The current collapse measurement conditions of the two devices no-buffer and standard were as follows: a pulse width of 2 µs and a duty cycle of 0.01%. The time waveform of the devices under a drain quiescent voltage(V_{DSQ}) of 30 V is depicted in Fig. 4(a).

The pulsed IV characteristics at different values of V_{DSQ} were measured on HEMTs for both devices in Fig. 4(b). The quiescent bias points (V_{GSQ}, V_{DSQ}) were set at V_{GSQ} = –3 V and V_{DSQ} = 0–30 V at a step of 10 V. The standard device exhibits a significant current collapse because of the electron-trapping effect of the deep acceptors in the buffer layer.

Therefore, the current collapse of the no-buffer device is lower than that of the standard device at a drain quiescent voltage of 30 V (V_{GSQ} and V_{DSQ} = –3 and 30 V, respectively).

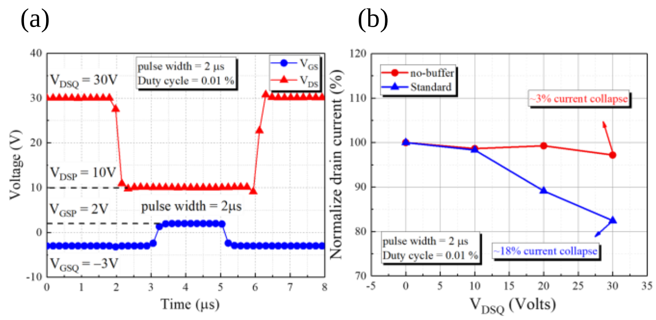

Fig. 4. (a) Waveform of operating time during pulse measurement. (b) Normalized Ron values under different V_{DSQ}.

To explore the influence of thermal boundary resistance and self-heating in a high-power state, the analysis of thermal image measurement is shown in Fig. 5. Surface temperature maps were obtained according to the infrared radiation intensity measured using an IRM P384G detector. Fig. 5(a) shows that the surface temperatures of the no-buffer and standard devices after operating at V_{DS} = 28 V and V_{GS} = 0 V for 30 s were 40°C and 58°C, respectively. The two devices were operated at a V_{DS} of 28 V, with a V_{GS} sweep from −2.5 to 0 V with a step is 0.5 V and a measurement time of 30 s, as shown in Fig. 5(b). Fig. 5(c) shows the graph of surface temperature and different P_{DC}. The no-buffer structure exhibits a lower temperature because the heat generated at high drain bias and high current would dissipate more efficiently into the substrate and then improve the reliability problem caused by the self-heating effect.

Fig. 6 shows the load–pull and two-tone characteristics of large-signal performance measured using the Maury high-frequency power parameter measurement system. The two devices were operated at a frequency of 3.5 GHz and a V_{DS} of 28 V, and the corresponding input power (P_{in}), output power (P_{out}), power gain, and power-added efficiency (PAE) relationship are displayed in Fig. 6(a). According to the results in Fig 6(a), for the no-buffer device at the peak PAE of 51.3%, the associated output power was 5 W/mm. For the standard device at the peak PAE of 49%, the associated output power was 4.2 W/mm. Referring to the previous DC and pulse measurements because the no-buffer structure has lower thermal effects and current collapse effects in a high-power state, better characteristics can be obtained in terms of PAE and output power performance.

The third-order intermodulation product of the device output spectrum and input RF power is an important indicator of device linearity. For this measurement, the operating frequency was 3.5 GHz and the tone spacing was 40 MHz (3.48 GHz and 3.52 GHz). Fig. 6(b) shows the results from the two-tone measurement. The third-order intercept point at the output (OIP3) was 41 dBm for the no-buffer device, and this value was 31.5 dBm for the standard device. The no-buffer structure is less affected by the intermodulation distortion than traditional devices.

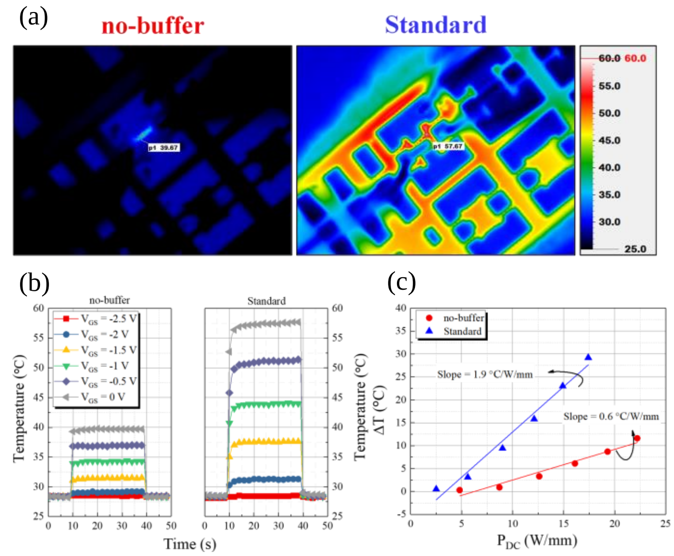

Fig. 5. The analysis of thermal image measurement of (a) no-buffer and standard devices. (b) Analysis of thermal behavior at V_{DS} = 28 V, with a V_{GS} sweep from −2.5 to 0 V, and (c) surface temperature at different P_{DC}.

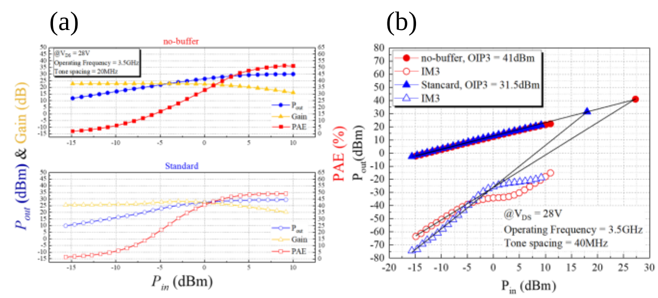

Fig. 6. (a) Load–pull measurement at V_{DS} = 28 V and 3.5 GHz. (b) Two-tone linearity measurements with operating frequency of 3.5 GHz and tone spacing of 40 MHz.

To measure the device lateral breakdown characteristics, we used the Agilent B1505A measurement system to measure the breakdown voltage of the no-buffer and standard structures. Device isolation was achieved by Ar+ implantation to locally remove the two-dimensional electron gas between two-terminal ohmic contacts. We covered the device with a fluorinated liquid (FC-40) during the measurement to prevent arcing in the air caused by the high electric field. The distance between the two-terminal ohmic contacts was 20 μm, and the schematic of the measurement is depicted in Fig. 7. Because of the high-quality AlN NL of the no-buffer device, which serves as the back barrier layer, and its material properties of a high-breakdown electric field, the lateral breakdown voltage of the device has been improved to 1995 V.

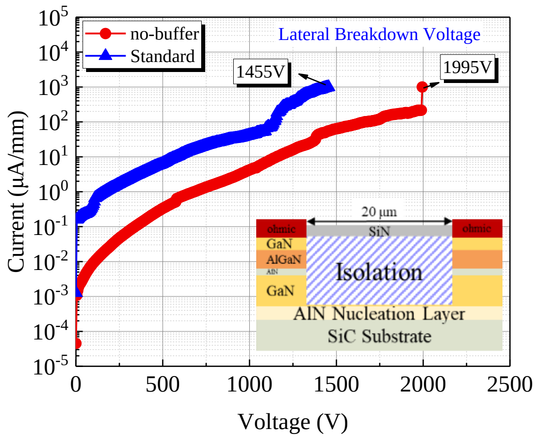

Fig. 7. The lateral breakdown voltage characteristics of no-buffer and standard devices.

Conclusions

This study analyzed the characteristics of AlGaN/GaN HEMTs grown on a no-buffer QuanFINE heterostructures. Based on the high-quality AlN NL structure, the scattering and thermal boundary resistance caused by the epitaxial quality of the traditional NL are improved. In addition, the measurement and analysis results show that the high-quality AlN NL and the no-buffer structure can reduce current collapse and self-heating under high-voltage and high-current conditions. The surface temperature measured by thermal image analysis has also been significantly improved by approximately 30%. Based on the above research results, the no-buffer device achieved high output power and linearity of large-signal performance, which opens many possibilities for millimeter-wave power amplifier applications.

References

[1] H. Chiu, S. Chen, "AlGaN/GaN Schottky barrier diodes on silicon substrates with various Fe doping concentrations in the buffer layers", Microelectronics Reliability, vol. 83, 2018, pp. 238-241.

[2] Y. Jia, Y. Xu, Senior Member, IEEE, K. Lu, Z. Wen, A. D. Huang, and Y. X. Guo, Fellow, IEEE, "Characterization of Buffer-Related Current Collapse by Buffer Potential Simulation in AlGaN/GaN HEMTs", IEEE TRANSACTIONS ON ELECTRON DEVICES, VOL. 65, NO. 8, AUGUST 2018.

[3] F. Jia, Graduate, X. Ma, L. Yang, B. Hou, M. Zhang, Q. Zhu, M. Wu, M. Mi, J. Zhu, S. Liu, and Y. Hao, "The Influence of Fe Doping Tail in Unintentionally Doped GaN Layer on DC and RF Performance of AlGaN/GaN HEMTs", IEEE TRANSACTIONS ON ELECTRON DEVICES, VOL. 68, NO. 12, DECEMBER 2021.

[4] J. G. Kim, C. Cho, E. Kim, J. S. Hwang, K. H. Park and J. H. Lee, "High Breakdown Voltage and Low-Current Dispersion in AlGaN/GaN HEMTs with High-Quality AlN Buffer Layer", IEEE TRANSACTIONS ON ELECTRON DEVICES, VOL. 68, NO. 4, APRIL 2021.

[5] J. Bergsten, M. Thorsell, D. Adolph, J. T. Chen, O. Kordina, E. Ö. Sveinbjörnsson and Niklas Rorsman, "Electron Trapping in Extended Defects in Microwave AlGaN/GaN HEMTs with Carbon-Doped Buffers", IEEE TRANSACTIONS ON ELECTRON DEVICES, VOL. 65, NO. 6, JUNE 2018.

[6] M. E. Villamin, T. Kondo and N. Iwata, "Effect of C- and Fe-doped GaN buffer on AlGaN/GaN high electron mobility transistor performance on GaN substrate using side-gate modulation", Japanese Journal of Applied Physics 60, SBBD17(2021).

[7] J. Lu, J. T. Chen, M. Dahlqvist, R. Kabouche, F. Medjdoub, J. Rosen, O. Kordina, and L. Hultman, "Transmorphic epitaxial growth of AlN nucleation layers on SiC substrates for high-breakdown thin GaN transistors", Appl. Phys. Lett. 115, 221601(2019).

[8] D. Y. Chen, A. Malmros, M. Thorsell, H. Hjelmgren, O. Kordina, J. T. Chen, and N. Rorsman, "Microwave Performance of 'Buffer-Free' GaN-on-SiC High Electron Mobility Transistors", IEEE ELECTRON DEVICE LETTERS, VOL. 41, NO. 6, JUNE 2020.

[9] J. T. Chen, J. Bergsten, J. Lu, E. Janzen, M. Thorsell, L. Hultman, N. Rorsman, and O. Kordina, "A GaN–SiC hybrid material for highfrequency and power electronics", Appl. Phys. Lett. 113, 041605(2018).

[10] N.V. Safriuk, G.V. Stanchu, A.V. Kuchuk, V.P. Kladko, A.E. Belyaev, V.F. Machulin, "X-ray diffraction investigation of GaN layers on Si(111) and Al_2O_3(0001) substrates", Semiconductor Physics, Quantum Electronics & Optoelectronics, 2013.

[11] I. Booker, L. R. Khoshroo, J. F. Woitok, V. Kaganer, C. Mauder, H. Behmenburg, J. Gruis, M. Heuken, H. Kalisch and R. H. Jansen, "Dislocation density assessment via X-ray GaN rocking curve scans", Phys. Status Solidi C 7, No. 7 – 8, 1787– 1789(2010).

[12] A. Manoi, J. W. Pomeroy, N. Killat and M. Kuball, "Benchmarking of Thermal Boundary Resistance in AlGaN/GaN HEMTs on SiC Substrates: Implications of the Nucleation Layer Microstructure", IEEE ELECTRON DEVICE LETTERS, VOL. 31, NO. 12, DECEMBER 2010.